ADVANCED FUNCTIONAL MATERIALS
www.afm-journal.de

# Laser-Induced Graphene from Waste Almond Shells

Yulia Steksova, Anna Chiara Bressi, Marina Galliani, Attilio Marino, Gianni Ciofani, Eduardo Machado-Charry, Hilda Gomez Bernal, Alessandra Francini, Luca Sebastiani, and Francesco Greco*

**Laser-induced graphene (LIG) is a 3D conductive carbon material typically produced from petroleum-based polymers via a one-step laser-induced pyrolysis in air, without chemicals. Recently, the focus has shifted toward bioderived and biodegradable precursors as potentially sustainable alternatives. Here, this approach is advanced by repurposing almond shells–an abundant raw agricultural by-product–blended with chitosan to form almond shell composites (ASC). ASC exhibits over 60% weight loss after 90 days under soil burial. It serves both as a bioderived substrate for electronics and as a precursor for LIG. ASC is converted into LIG through UV and IR laser scribing, and its structure is thoroughly investigated. ASC-LIG achieves sheet resistance values as low as 114.3 ± 0.9 Ω sq$^{-1}$ (UV), and an electrochemical impedance modulus $|Z| \approx 1$ kΩ at $10^6$ Hz (1 cm$^2$ electrodes). It is implemented in proof-of-concept electronic devices, including circuits with resistive and capacitive elements, and humidity sensors, which show sensitivities of 2.25 ± 0.13 pf%RH$^{-1}$ (30%–55% RH) and 19.8 ± 2.69 pf%RH$^{-1}$ (55%–80% RH). These results highlight the potential of upcycling agricultural by-products into functional materials, demonstrating the suitability of ASC-LIG for transient electronic applications such as environmental sensors.**

## 1. Introduction

In recent years, there has been a growing interest in developing sustainable and degradable materials for electronics, driven by the need to reduce environmental impact and create innovative technologies that can replace traditional, non-degradable materials. Opportunities in this direction can be offered by laser-induced graphene (LIG), a 3D porous and conductive carbon structure obtained by laser-induced pyrolysis of synthetic polymers such as polyimide,[1] as well as bioderived polymers or biomass-based materials.[2–5] LIG has attracted the attention of researchers due to its good conductivity, high porosity, ease of processing, and the ability to be modified to suit various technological tasks.[6–8]

The application of LIG has gained relevance in the context of zero-waste electronic technologies, where circularity and biodegradability are key challenges for future electronics development.[9] Recently, LIG has been used as the sensitive element in a variety of flexible/stretchable sensors. Some examples include soft, skin-interfaced electrodes and strain sensors,[10,11] electrochemical sensors to monitor uric acid, tyrosine and pH in human sweat,[12] strain sensors in soft robotics,[13,14] and environmental sensors for monitoring temperature, gas, pressure, humidity, levels of pollutants in the air or water, etc.[15,16] Originally, mainly synthetic polymer substrates were used to form LIG,[1] but the production of LIG from bioderived

---

Y. Steksova, A. C. Bressi, M. Galliani, H. G. Bernal, F. Greco
The Biorobotics Institute and Dept. of Excellence in Robotics & AI
Scuola Superiore Sant'Anna
Viale R. Piaggio 34, Pontedera 56025, Italy
E-mail: francesco.greco@santannapisa.it

A. Marino, G. Ciofani
Center for Materials Interfaces
Electron Crystallography
Istituto Italiano di Tecnologia
Viale R. Piaggio 34, Pontedera 56025, Italy

E. Machado-Charry
Institute of Solid State Physics
NAWI Graz
Graz University of Technology
Graz 8010, Austria

A. Francini, L. Sebastiani
Institute of Crop Science
Scuola Superiore Sant'Anna
Piazza Martiri della Liberta 33, Pisa 56127, Italy

F. Greco
Interdisciplinary Center on Sustainability and Climate
Scuola Superiore Sant'Anna
Piazza Martiri della Libertà 33, Pisa 56127, Italy

The ORCID identification number(s) for the author(s) of this article can be found under https://doi.org/10.1002/adfm.202507462

**DOI: 10.1002/adfm.202507462**

materials quickly emerged as an interesting alternative.[17] The use of bioderived substrates to form LIG has been widely reviewed and mainly focuses on cellulose and lignin-based materials. Recent articles have explored laser-induced graphene formation from both synthetic and natural materials, highlighting differences in morphology, graphitization, and application potential depending on the laser process type and substrate used.[18] In view of the sustainable production of green electronics, the use of waste biomass as LIG precursors and as device substrate may represent a step forward in reducing the environmental impact of electronics. Lignin is one of the main components of plant-derived materials and dominates forestry and agricultural products and by-products, such as wood residues, nut shells, and husks. By-products of biomasses are globally produced in huge volumes, and there is a great interest in converting them into added-value functional materials.[19] Lignin is also reported as one of the best precursors for LIG,[3] often in combination with cellulose, as typically found in plant-derived materials. A high content of lignin has been correlated with high quality of the LIG produced from different types of wood, in terms of crystalline carbon formation and low sheet resistance.[17] LIG derived from lignin and more broadly from plant biomass offers a potentially environmentally friendly alternative to synthetic carbon materials,[20] particularly for the development of flexible and degradable electronics.[21–23] Advances in wood-based biodegradable electronics highlight the feasibility of converting lignocellulosic biomass into functional printed devices, such as eco-friendly transistors for neuromorphic or sensing applications.[24] However, the use of these plant-derived LIG precursors often requires a complex processing: the extraction/purification of lignin or other polymeric precursors from raw bioderived materials, the use of inert or reducing atmosphere during laser scribing, a pretreatment with flame retardants and/or catalytic agents, such as iron-based inks, or a multi-step laser scribing procedure.[25,26] This complex and often energy-intensive processing could, at least in part, hamper the use in real applications and negatively impact the overall environmental impact. Finding strategies to reduce the processing burden is thus of paramount importance in the aim of creating more sustainable technologies. In this sense, the use of raw, unprocessed, or minimally processed by-product materials should be preferred over compounds that are extracted and purified. Nutshells, such as those of pistachios, hazelnuts, and almonds, are particularly abundant by-products of the agricultural and food industries. The shells represent a very large part of the crop's yield, i.e., in almonds, 67% in weight.[27] Given the large number of agricultural inputs and natural resources for growing nuts, and considering that most of the yield is commonly wasted or poorly valorized, there is space for improving their overall environmental and economic sustainability.

In our study, we focused on the use of almond shells (AS) by-products, since almonds are one of the most cultivated nuts in the world: their demand has increased almost 6 times over the past 20 years,[28] and the global annual production volume of shells is ≈800 000 tons.[29] Such a volume of by-products requires the adoption of effective valorization methods. Most of these shells are currently used as energetic biomass (e.g., combustible for ovens) or mulching substrate for gardening, with very low market value (around 6–10 cents kg$^{-1}$ in Italy; Damiano S.p.A., personal communication: March 2022). For these reasons, there is a huge interest in recycling this biomass by including it in the formulation of biocomposites[30,31] or transforming it into added-value functional materials like adsorbent materials and activated carbon, among others.[32–35]

Depending on the almond cultivars, the shells may contain 30–40 wt.% lignin and 25–30 wt.% cellulose and hemicellulose,[36–38] thus nutshells are potentially ideal to produce LIG.

Our aim was not only to investigate AS as a precursor for LIG, but also to provide strategies to transform AS into a bioderived substrate for electronics, in view of their applications in green electronics. To these aims, we first investigated the composition of two types of AS. Indeed, various almond cultivars exist, with different properties and composition of their shells. Almond cultivars are categorized into "hard shell" (high density ≈ 480 kg m$^{-3}$) and "soft shell" (low density ≈ 350 kg m$^{-3}$), which may have different relative concentrations of lignins, cellulose, and hemicelluloses.[31,39]

The powders of the two types (H-ASP and S-ASP, respectively for hard and soft types) were used as fillers for the realization of composite films with chitosan, a polysaccharide extracted from animal waste (e.g., crabs and arthropods' exoskeletons), acting as the matrix, or continuous phase of the composite.[40] The use of polysaccharides as a matrix to compound various bioderived fillers has become increasingly popular as a potentially more sustainable option compared to petroleum-derived polymers. Among the most common polysaccharides, starch, chitosan, pectin, alginate, and cellulose have been proposed in various applications.[41–46] They have several advantages: biocompatibility, degradability, ease of modification, non-toxicity, and good mechanical characteristics. Chitosan, adopted in our study, can be processed into various shapes, including porous structures, thin films, gels, membranes, and fibers. Moreover, recent studies demonstrated that chitosan itself can be converted into LIG by laser irradiation.[47] However, it is worth noting that the production of LIG from pure chitosan (i.e., without the use of reinforcing materials or additives) requires a complex three-step laser irradiation process using different types of lasers.

In this study, instead, we focused on developing chitosan composites with a large concentration of ASP, which accounts for more than 2/3 of the total mass of powder components. The AS chemical composition and its effect on the mechanical properties of almond shell composite (ASC) were studied, providing a basis for critical selection of the most promising AS type to use as filler. A particle size analysis of the ASP was carried out, and then ASC morphology was analyzed using optical microscopy and scanning electron microscopy (SEM). The degradability in soil of ASC was assessed by mass loss and Fourier transform infrared spectroscopy (FTIR).

LIG was obtained from ASC through direct scribing with either an ultraviolet (UV) or an infrared (IR) laser. Each type of laser has a different effect on the material, leading to the formation of different microstructures and properties of LIG, which were studied in detail through SEM, Micro-CT, and Raman spectroscopy. An optimization of the laser parameters was carried out to achieve the lowest sheet resistance. LIG-based electrical circuitry elements and a proof-of-concept humidity sensor were fabricated on ASC, demonstrating their potential for use in potentially sustainable and degradable printed circuit boards.

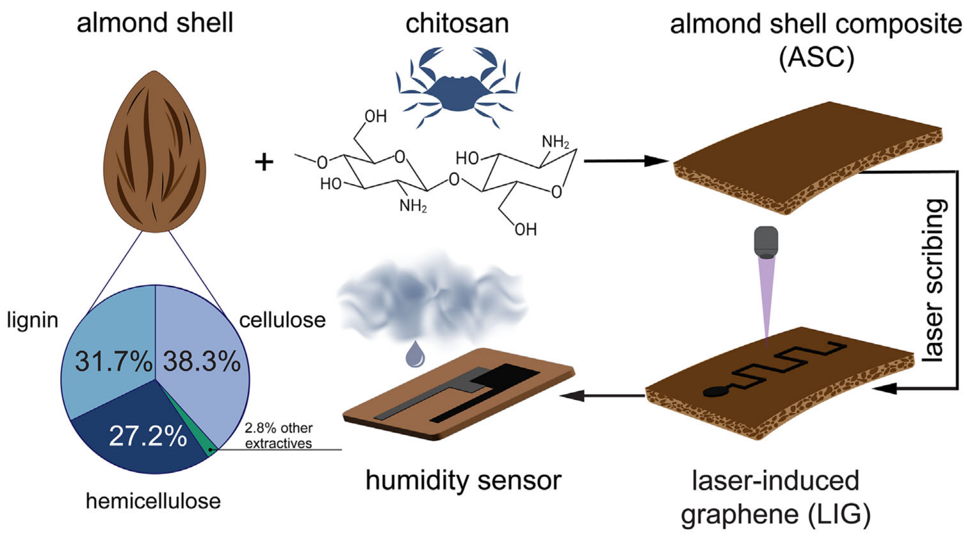

**Figure 1.** Schematic overview of the study. Synthesis of the Almond Shell Composite (ASC) from waste almond shell powder (ASP) (composed of lignin, cellulose, and hemicelluloses) and chitosan, followed by laser scribing of LIG conductive patterns and potential use as a capacitive humidity sensor.

## 2. Results and Discussion

The results section includes four main parts, and a schematic overview of the overall study is shown in **Figure 1**.

The first section presents the chemical composition analysis of the two types of biomass powder, H-ASP and S-ASP, in terms of their cellulose, lignin, and hemicellulose content.

The second section details the synthesis of ASC based on ASP, chitosan, and glycerol, followed by an evaluation of the ASC mechanical and degradability properties.

The third section describes the laser-assisted scribing of LIG on the surface of ASC (ASC-LIG) and analyzes the differences in its properties when obtained with an IR or a UV laser.

Finally, the last section demonstrates the fabrication of ASC-LIG flexible transient electronics, such as capacitors and resistors, and a humidity sensor.

### 2.1. Almond Shell Powder (ASP) Characterization

The chemical composition of almonds can exhibit significant variability, not only among different almond varieties but also within the same variety. These differences can be influenced by several factors, including geographical origin, climatic conditions, agricultural practices, and the year of the crop.[48] It is fair to assume that the shells, and thus the resulting ASP, are also subjected to these variations. Understanding these changes is crucial for characterizing the properties of specific ASP samples, ensuring the reproducibility of the results. Moreover, the ASP chemical composition plays a key role in determining the ASC properties (e.g., mechanical, moisture absorption) and the possibility of using it as a precursor for LIG in direct laser writing pyrolysis. The cellulose content of the almond shells used in this study was found to be 38.7 ± 0.40% for the S-ASP and 37.8 ± 0.57% for the H-ASP, in line with literature values.[39] Cellulose content in almond shells is higher than that of other shells, such as walnut, hazelnut, chestnut, and pine shells, but lower than pistachio and coconut.[39,49–51] Cellulose has a significant effect on the mechanical properties of the composite, contributing to their overall enhancement.[52]

On the other hand, almond shells also have high lignin content: 30.6 ± 0.34% for the S-ASP and 32.7 ± 0.43% for the H-ASP. This is advantageous because lignin, even better than cellulose, is known to be a good substrate for LIG.[53,54]

The hemicellulose content is the same for both H-ASP and S-ASP, 27.2 ± 0.23% and 27 ± 0.25%, respectively. Hemicellulose, being amorphous, gives flexibility and elasticity to almond shells; it serves as a link between cellulose and lignin, improving the interaction between them.[39,55]

Considering the results obtained, the general chemical composition of H-ASP and S-ASP is overall similar. A comparative analysis of the cellulose, lignin, and hemicellulose content in several types of nut shells is given in the Supporting Information (Table S1, Supporting Information).

A granulometry analysis of ASP was carried out through an automatic shape recognition software tool on optical microscope images. It permitted the evaluation of ASP particle size distribution after grinding and sieving. Representative microscopic images of an S-ASP sample before and after the application of the automatic shape recognition software tool are reported in Figure S1a,b (Supporting Information), respectively. While a perfectly dispersed mixture was not achieved and some agglomerates remained, most were excluded by the software. Most of the ASP samples, both H-ASP and S-ASP, consist of particles with a diameter < 5 µm (Figure S1c, Supporting information). A normalization based on particle volume rather than particle count lets a different distribution pattern emerge (Figure S1d, Supporting information), indicating that, although fewer, larger particles are significant due to their greater volume. The percentage values may not be of primary concern for our study, but the consistency of results across different samples guarantees the reliability of the grinding process. This consistency is critical for composite manufacturing, as different granulometry corresponds to

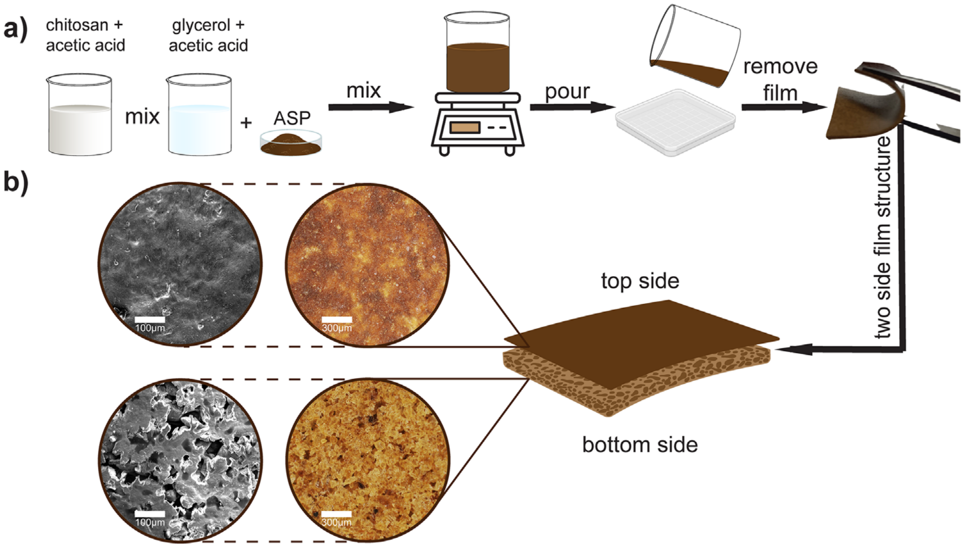

**Figure 2.** a) ASC synthesis schematic: the blend containing ASP, a solution of glycerol + acetic acid, and a solution of chitosan + acetic acid is mixed and then cast to obtain the ASC film. b) ASC structure with images of the top and bottom surfaces (left SEM images, right optical microscope images).

a different surface-to-volume ratio, and this may influence the particle-particle and particle-matrix interfaces. Granulometry can thus affect the compactness, porosity of the composite, and the binding properties of the continuous phase of the composite-in this case, the chitosan polymer.

## 2.2. Almond Shell Composite (ASC)

### 2.2.1. Microscopic Morphology

Almond Shell Composites (ASC) are obtained using chitosan as a matrix, ASP as a reinforcement, and glycerol as an additive. Both H-ASP and S-ASP are used for ASC manufacturing, leading to H-ASC and S-ASC, respectively. The choice of ASP contributed to differences in the morphology of the composites. H-ASC has many powder clusters on the bottom side, which can probably be attributed to the distribution of powder particle sizes after milling. Indeed, according to the granulometry results, H-ASP and S-ASP have different distributions of particle size (Figure S1, Supporting Information).

During composite preparation (**Figure** 2a), at the drying stage, we observe the accumulation of almond powder (brown) at the bottom of the cast mixture, and the resulting film presents a layered structure (Figure S2, Supporting Information).

The morphology of the resulting S-ASC is shown in Figure 2b. The composite has a distinct two-layer structure with a clear stratification of particles at the bottom. This granular morphology is due to the ASC synthesis process. Indeed, the long 18-h drying step allows the ASP particles dispersed in the liquid mixture to stratify based on a size gradient. Bigger and heavier particles tend to settle at the bottom, while finer particles accumulate at the top. The top surface is darker and smoother, and it is richer in glycerol, which interacts with the finer ASP particles, also inducing their swelling, which consequently decreases their density.[56] Accumulation of glycerol promotes the sedimentation on the top layer, filling the gaps between the ASP and creating a more homogeneous structure, ultimately forming a thin film that “glues” the material.

The bottom surface has a less dense, more granular, and rougher structure due to the accumulation of larger almond shell powder granules during the drying process.

### 2.2.2. Mechanical Test

Mechanical tests are conducted to assess the influence of the ASP addition to the chitosan matrix in terms of Young’s modulus E and tensile elongation at break $\varepsilon_{max}$ (Table S2, Supporting Information). The results of mechanical tests show that the rigidity of ASC increases significantly compared to pure chitosan film, having $E = 2.45 \pm 0.06$ MPa. In particular, H-ASC shows a slightly higher $E = 18 \pm 1.64$ MPa compared to the S-ASC $E = 13.97 \pm 0.51$ MPa (**Figure** 3a), which confirms the influence of the chemical composition of the shell on the rigidity of the material. At the same time, the addition of ASP also reduces the maximum elongation at break for both H-ASC and S-ASC ($\varepsilon_{max} \approx 10\%$) with respect to chitosan ($\varepsilon_{max} \approx 55\%$), indicating an increased brittleness of the film. These changes are associated with the hydrophobic properties of the almond shell, which prevent plastic deformation and reduce the ductility of the material.[57]

These results are in line with the literature,[58] in which an increase in the content of ASP in biopolymer materials leads to a significant increase in Young’s modulus. Another study[59] reveals that the incorporation of 5%–20% ASP into a starch-based film slightly increases the E, while drastically decreasing the impact resistance, the tensile and flexural strength at break.

It is worth noting that the mechanical properties of chitosan film vary depending on the amount and concentration of glycerol. For example, when adding glycerol, the tensile strength decreases, making the film more elastic and flexible. Glycerol acts as a plasticizer, weakening intermolecular interactions in

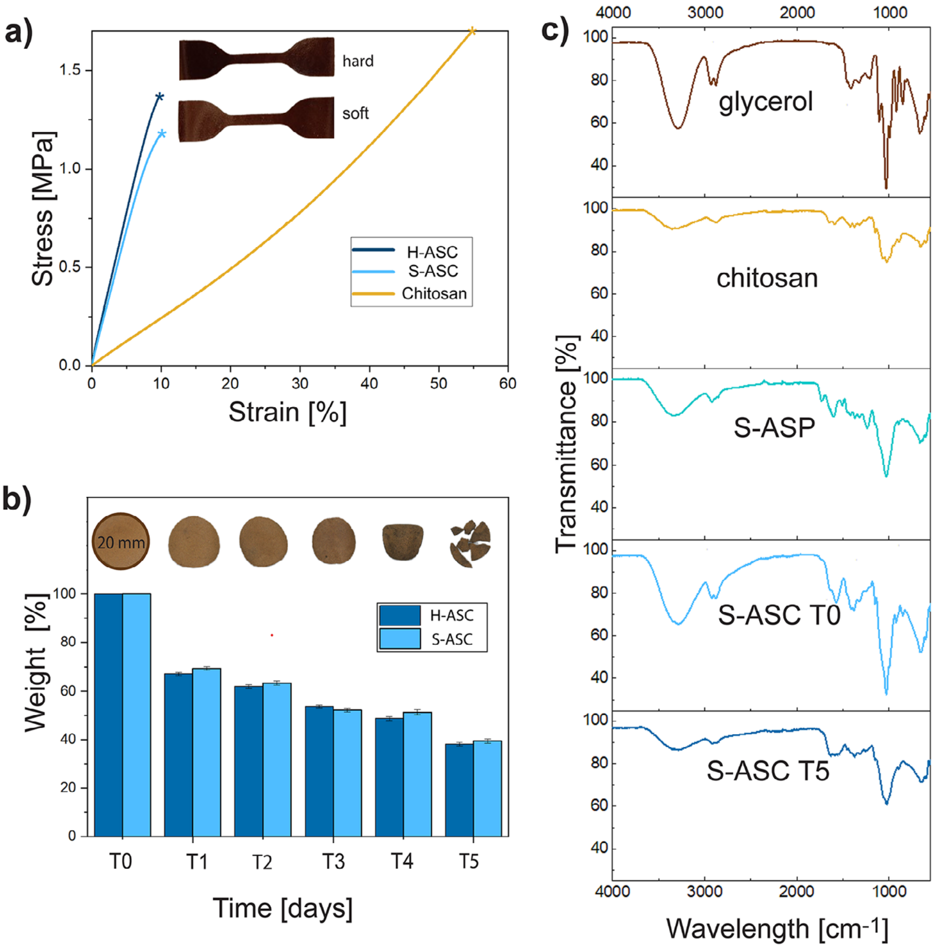

**Figure 3.** a) Stress–strain curves for H-ASC, S-ASC and Chitosan film; b) Weight (wt.%) of H-ASC and S-ASC vs. time during degradation in soil and corresponding images of the degraded S-ASC samples at different time points: *T0* = 0, *T1* = 2, *T2* = 8, *T3* = 20, *T4* = 40, *T5* = 90 days; c) FTIR spectra of the composite ingredients and of S-ASC samples at time *T0* and *T5* during the degradation process (details in Figure S4 and Table S3, Supporting Information).

chitosan and increasing the mobility of the polymer chains.[60] Also, when adding plasticizers, E decreases, which indicates a decrease in film rigidity, while increasing the elongation at break, making the film more elastic and flexible. For example, the use of 20% glycerol in chitosan/polyethylene oxide resulted in a decrease of the tensile strength from 24.74 to 2.91 MPa.[61]

The ASC remained quite flexible for several months after preparation. Samples stored in ambient conditions (exposed to air, light, and temperature variations in a non-closed container) for around 12 months became brittle and stiffer. Some cracks appeared in the same timeframe, despite the film retaining its overall integrity. We attribute this to the gradual loss of moisture or migration of components such as glycerol. Some images of samples immediately after preparation and after 12 months are shown in Figure S3 (Supporting Information).

### *2.2.3. Degradation Test*

The degradability of ASC in soil was studied to demonstrate the potential use for further application of these composites in transient/green electronics, as bioderived materials may be an optimal choice for environmental sensor substrates capable of monitoring various parameters (temperature, humidity, etc.).[62]

Figure 3b shows all stages of sample degradation in soil. After 90 days (T5) in the soil, the H-ASC and S-ASC samples lost more than 60% of their mass.

In order to investigate the degradation process, FTIR spectra of the ingredients of ASC (chitosan, glycerol, and ASP) were obtained, along with the spectra of S-ASC samples at every time point of the degradation test T0-T5 (Figure 3c). For FTIR spectra of each of the S-ASC components, we identified the relevant bands, described in more detail in the Supporting Information section (Figure S4 and Table S3, Supporting Information).

At the initial stage, in the S-ASC T0 sample, the FTIR spectrum reflects the presence of all the ingredients. Pronounced peaks in the region of 3500–3300 cm$^{-1}$ indicate the presence of OH groups characteristic of glycerol and cellulose, as well as amide groups inherent to chitosan (peaks around 1646 and 1321 cm$^{-1}$). Also, the peak at 1026 cm$^{-1}$, corresponding to C—O stretching, indicates the presence of cellulose and glycerol. As the sample degrades, a significant decrease in the intensity of the peaks associated with glycerol and chitosan is observed (T5). Particularly noticeable is the decrease in the intensity of the peaks in the range of 1700–1400 and 995–850 cm$^{-1}$, which indicates the leaching of glycerol and the degradation of chitosan. The change in spectra may also indicate the destruction of amide structures, which leads to the decomposition of these components. A decrease in the intensity of the peaks in the C—H region (2925 and 2877 cm$^{-1}$) confirms that both glycerol and chitosan are decomposed during the process, which leads to a significant change in the chemical composition of the composite. Moreover, the change in structure in the 1700–1400 cm$^{-1}$ region, as well as weak peaks in the 850 cm$^{-1}$ region, indicate that decomposition of almond shells and other biomass components also takes place. Overall, around 40% of mass is retained after 90 days. It is reasonable to assume that this leftover mass is mainly constituted of ASP filler, for which a complete degradation is expected at longer times. Indeed, in the case of degradation of pure almond shells, mass loss is up to 55% in 360 days.[63] Chitosan, instead, is readily degradable in soil, like other polysaccharides.[64]

### 2.3. Laser-Induced Graphene from ASC

The main objective of this study was to create ASCs to be used as substrates and precursors for LIG. A compromise was thus required between good mechanical properties, such as flexibility and integrity under load, as provided by the matrix chitosan-and a high amount of lignin-rich filler, thought of as a good LIG precursor. Based on the results of the studies of composites, as well as some preliminary scribing tests, the S-ASC type was selected for further work on LIG scribing. The full comparative analysis presented in Table S4 (Supporting Information) summarizes the main differences between S-ASC and H-ASC in terms of the ASP granulometry, sheet resistance, Raman performance, and mechanical properties, and provides the rationale for choosing S-ASC as the LIG precursor for further investigations. Another factor taken into account was the ASC thickness. Based on an initial screening, a thickness of 0.6 mm was found to be optimal. Indeed, a larger thickness was unnecessary and could reduce the overall substrate flexibility. On the other hand, thinner ASCs would risk being perforated or structurally compromised due to laser beam exposure during the scribing process. The selected thickness ensures sufficient ASC conversion into LIG on the surface, while maintaining mechanical support and homogeneity in the bottom part of the composite. The same ASC thickness was maintained across all samples, apart from the vertical capacitor used as a sensor, where a thicker (1.2 mm) ASC was used. The study on LIG formation is performed for both sides of the S-ASC composites, with significant differences due to the stratification of the composite discussed in the previous section. Such structural features of the composite significantly affect its further transformation into LIG. In addition, the difference in heat dissipation during laser processing of the top and bottom sides, as well as differences in UV or IR absorption and subsequent photochemical modification of the surface, also cause differences in the resulting LIG.

In the case of UV laser irradiation, surface graphitization is successful on both surfaces. In the case of IR laser irradiation, surface graphitization is successful only on the bottom surface, while just ablation occurs on the top surface. Due to these differences, the bottom side of the ASC was chosen as a substrate for further optimization of the laser parameters and study of the LIG structure.

The sets of laser scribing parameters have been screened and optimized for the two types of lasers used. For UV laser, the set included power ($P$), speed ($S$), Q-switch frequency CW, fill interval, and laser-scribing direction parameter (pattern). For IR, the set included P, S, focus ($Z$), number of scribing repetitions ($N$), resolution ($PPI$), and image density (i.e., distance between successive raster lines). Optimized scribing protocols for such parameters (reported in Experimental section) were created for H-ASC and S-ASC separately, with an emphasis on obtaining LIG with the best conductivity (i.e., lowest sheet resistance $R_s$).

UV-scribed LIG (UV-LIG) showed a minimum sheet resistance $R_s = 114.3 \pm 0.9\ \Omega\ \text{sq}^{-1}$ on the bottom side and $R_s = 91 \pm 10.1\ \Omega\ \text{sq}^{-1}$ on the top side. It is important to notice that for UV, the optimized parameters included focused conditions ($Z = 0$ mm) and a “cross” scribing (i.e., alternate scribing along x and y axes on the plane). This method increased the number of laser action points on the substrate. **Figure 4a** shows the scribing scheme using the cross-scribing method for UV.

IR scribed LIG (IR-LIG) showed a minimum $R_s = 1.57 \pm 1.0 \text{ x } 10^3\ \Omega\ \text{sq}^{-1}$. The results show that the focus Z had a great influence on the final result; in the case of the IR laser, a systematic optimization was carried out by adopting a “wedge” setup,[65] which allowed the laser focal length to be continuously increased in the range of $Z = 0$–5 mm along the length of the sample during raster scribing. Also, it is important to notice that for IR, the optimized parameters included a defocused condition ($Z = 5$ mm) and 3 scribing repetitions. The scribing repetition scheme for IR is displayed in Figure 4f. A larger number of repetitions caused the destruction of the composite.

To confirm the hypothesis that ASP is the real LIG precursor in ASC, a chitosan film, not including any ASP, was also laser scribed, trying to optimize the laser scribing settings described above. Local melting and ablation of the chitosan occurred when irradiated with both IR and UV lasers, without the formation of any carbon-like structure (Figure S5, Supporting Information). In our case, we tried to use a simple one-step (one laser only) scribing process to obtain LIG, which, however, could not be obtained from chitosan-based films. A recent study demonstrated the possibility of obtaining LIG from chitosan films, but in that case, a complex three-step laser irradiation was used, with preliminary material treatment with a low-power IR laser, further exposure to a diode laser, and a final stage of high-power IR laser processing.[66] In another example, a chitosan film,[47] containing only chitosan, acetic acid, glycerol, and water, as in the present study, could be converted into a porous 3D graphene with a different three-step laser fabrication method. The process included irradiation with an IR laser (10.6 µm, 2.1 W) and visible (405 nm, 0.5 W) laser engravers. Since our primary objective was not to obtain LIG on chitosan but rather to maintain the same LIG scribing process used for ASC to demonstrate the key role of ASP– which was successfully confirmed – exploring complex alternatives for scribing LIG on chitosan-only films was not deemed necessary.

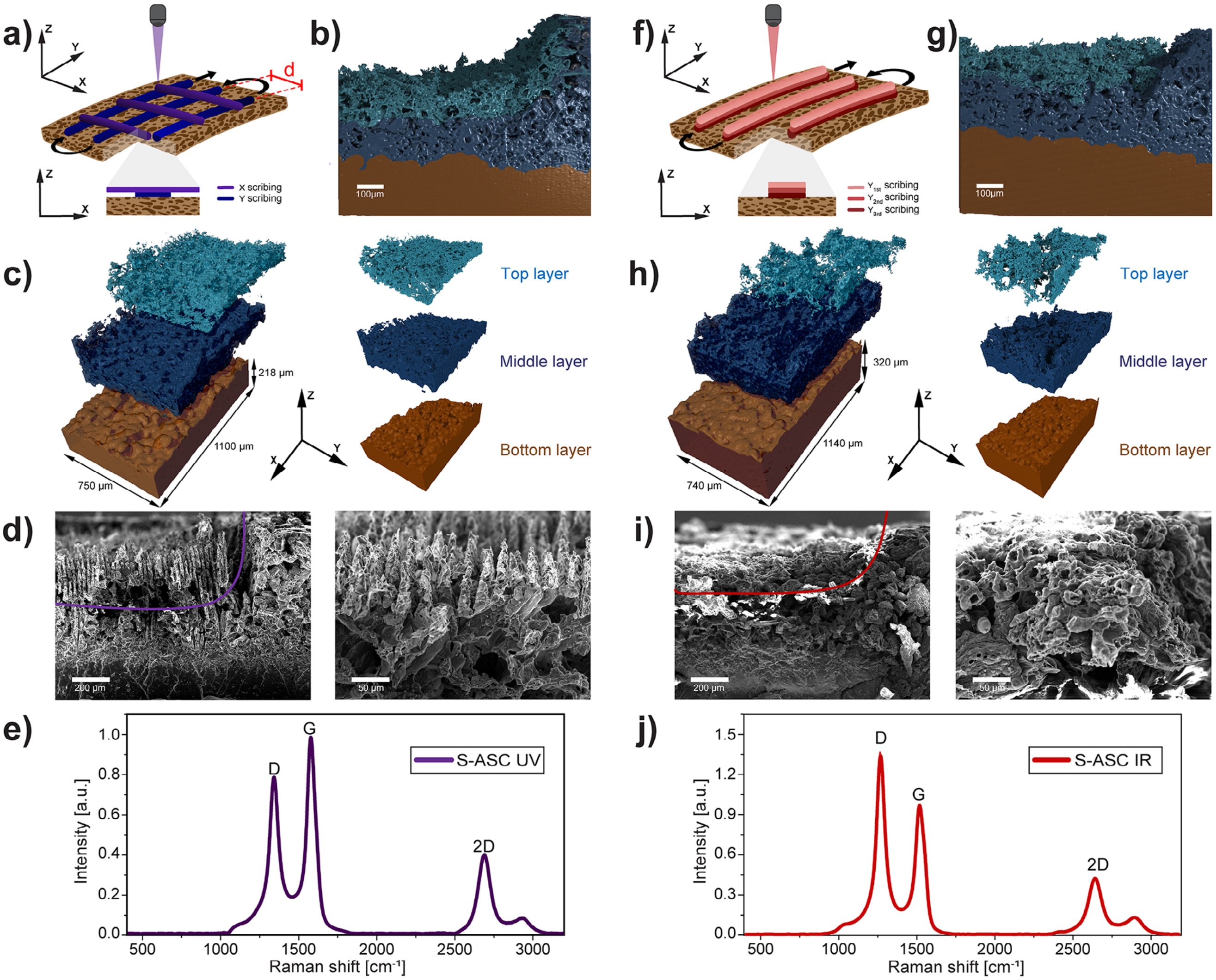

**Figure 4.** Laser-Induced Graphene from ASC. a) UV laser scribing scheme using the cross-patterning method (left → right, right → left). The distance *d* represents the fill interval parameter. b) cross-sectional micro-CT image along the xz plane of the UV-LIG. c) 3D image reconstruction by micro-CT of UV-LIG layers (light blue – top layer, dark blue – middle layer, brown – bottom layer). d) SEM images of UV-LIG. Left: cross-sectional view at the border zone, with purple line marking the boundary between the LIG and the pristine ASC. Right: cross-sectional view evidencing needle-like structure of the LIG top layer. e) UV-LIG Raman spectra (average over 3 spectra, standard deviations as shaded areas). f) Laser scribing repetition scheme for IR-LIG. g) Cross-sectional micro-CT image along the xz plane of the IR-LIG. h) 3D image reconstruction by micro-CT of IR-LIG layers (light blue – top layer, dark blue – middle layer, brown – bottom layer). i) SEM images of IR-LIG. Left: cross-sectional view at the border zone, with red line marking the boundary between the LIG and the pristine ASC. Right: cross-sectional view of the "foamy" mixed structure of the LIG top layer. j) IR-LIG Raman spectra (average over 3 spectra, standard deviations as shaded areas).

### *2.3.1. SEM and Micro-CT*

To study in detail the structure of the obtained LIG, scanning electron microscopy (SEM) analysis was performed. Figure 4d,i shows the cross-sectional microstructures of the laser-scribed ASC (laser scribing performed on the bottom surface of the composite) for UV and IR, respectively. The carbonized structure produced by UV laser scribing (Figure 4d) has a needle-like structure at the top, with each needle having a layered structure. The average distance between consecutive needles is 24.3 µm, which corresponds to a laser fill interval of 25 µm (needle dimensions and inter-needle spacing are shown in Figure S6, Supporting Information). Below this, a second layer is clearly visible, which consists of a continuous “foamy” mixed structure. It can be assumed that this layer, in addition to graphene, contains amorphous carbon and other carbon forms. In the case of IR laser scribing, no needles are evidenced in SEM (Figure 4i), and the structure exhibits a distinct single-layer “foamy” dense graphene configuration, which may also include various forms of carbon.

A detailed structural analysis of the materials, including the native ASC substrate and the graphitized parts, has been performed through micro-CT imaging. A similar study has been carried out on LIG from other precursors in a recent study,[26] which permitted highlighting the porosity and layered structure of LIG, correlated with the Heat Affected Zone (HAZ) induced by laser scribing.

The 3D image reconstructions obtained from micro-CT images of the UV-LIG (Figure 4b,c) and of the IR-LIG (Figure 4g,h) display the structural transformations obtained upon scribing on the pristine ASC material (evidenced in brown). The laser-affected areas display a layered structure: a top layer (light blue) and a middle layer (dark blue).

Notably, the surface area of the carbonized region differs between the two laser types: the UV-scribed structure has a thickness $t_{UV\text{-}LIG} \approx 300$ µm, approximately half the one of the original composite ($t = 730$ µm). The thickness of the IR-scribed structure $t_{IR\text{-}LIG} \approx 240$ µm, is significantly smaller, indicating a lower penetration depth of the IR laser into the substrate, despite the 3 repetitions. Furthermore, both UV and IR types exhibit a peculiar transition zone, the boundary between the graphitized region and the composite.

For UV-LIG, at the boundary of the scribed area (cross-sectional micro-CT image along the xz plane, Figure 4b on the right), the effect of laser irradiation (and thus HAZ) is incomplete; thus, a smaller ablation is observed along the rim. Also, the porous graphitized material (evidenced in light blue) is limited to a slightly smaller thickness compared to the rest of the scribed area. In the central part of the scribed area (Figure 4b, on the left), where energy is applied more evenly, the penetration depth and ablation are greater. The scribed area has a layered structure. Here, a highly porous LIG top layer is clearly distinguished, followed by a denser LIG middle layer with a mixed carbon structure, while the bottom layer is the pristine ASC.

A detailed study of the Micro-CT 3D images (Figure 4c) at the central part of the scribing area for the UV-LIG identifies significant changes in the microstructure. The top layer (light blue) has a thickness of $t_{UV\,top} = 80$–$120$ µm; exposed to intense laser radiation, it is more graphitized and consists of multi-layered graphene sheets with a highly porous, rough structure. As we move deeper inside the material, the carbon structure becomes smoother and denser. The middle layer (dark blue), which is denser and more heterogeneous than the top, has a thickness of $t_{UV\,mid} = 140$–$200$ µm. It probably combines graphene, amorphous carbon, and other carbon forms. This structure results from both the lower intensity of the laser exposure and the inherent morphological features of the pristine composite. As mentioned previously, the ASP accumulates in the lower part of the Petri dish during the drying process, forming a two-layer composite structure. Because scribing is performed on the bottom part, the high concentration of powder on the surface quickly either is ablated (hence the evident reduction in thickness) or turns into a porous graphenic carbon. The bottom layer (brown) is the pristine top layer of ASC unaffected by the laser, with a residual thickness $t \approx 210$ µm, out of the initial $t = 730$ µm. Thus, the ablation accounts for around 220 µm. For a more detailed analysis of the porosity of each layer, we used Otsu's thresholding algorithm, separating the foreground and background. The porosity assessment showed a decrease in porosity values from the top to the bottom layer of the UV laser-scribed ASC, from ≈ 76.52% in the top layer to ≈ 34.54% in the middle layer and ≈ 0.02% in the bottom layer (corresponding approximately to the top layer of ASC).

A similar analysis was also performed for the IR-LIG samples. The boundary of laser action for the IR laser (Figure 4g, on the right) is less pronounced than for the UV laser, and the boundary zone encompasses only the middle layer, without the highly porous top graphene layer. The latter is only displayed in the central part of the scribed area (Figure 4g, on the left) and occupies a smaller volume compared to the UV case, having a thickness of $t_{IR\,top} \leq 50$ µm (Figure 4h). The middle layer thickness of $t_{IR\,mid} = 220$–$300$ µm is thicker than the corresponding layer in the UV structure. The bottom layer (brown) is the pristine top layer of ASC unaffected by the laser, with a residual thickness of $t \approx 330$ µm, out of the initial $t = 730$ µm. Thus, the ablation accounts for around 100 µm, much less compared to the UV case. The porosity values measured in the IR-scribed structure show a similar trend to the UV-scribed sample, with porosity decreasing from 81.75% in the upper layer to 33.86% in the middle layer. The bottom layer retains the same porosity as the top layer of ASC, unaffected by the laser scribing.

In summary, we can conclude that the type of laser used for scribing (and the consequent difference in number of laser steps needed) has a significant effect on the structural evolution of LIG, as well as on its porosity and thickness. UV-LIG is characterized by high porosity and a thicker overall carbonized layer (top + middle) compared to IR-LIG. The thickness and porosity of the carbonized layers directly impact the material's properties, suggesting that UV-LIG is more suitable for applications requiring high conductivity, such as sensors. This, however, comes at the expense of a much higher ablation, so that less pristine ASC remains as a supporting substrate.

### 2.3.2. Raman Spectroscopy

The chemical structure of LIG obtained from S-ASC through both UV and IR laser scribing was studied by Raman spectroscopy Figure 4e,j (Raman spectra for the H-ASP sample in Figure S7, Supporting Information). All spectra show the three characteristic bands of graphene-based materials at around 1335 cm$^{-1}$ (peak D), 1580 cm$^{-1}$ (peak G), and 2670 cm$^{-1}$ (peak 2D). A strong D band-due to a breathing mode forbidden in perfect graphene-highlights the presence of lattice defects. The 2D band is obtained from the stacking of graphene sheets along the out-of-plane axis and is associated with the properties of multilayer graphene.[17,67,68]

The band intensity ratios $I_D/I_G$ and $I_{2D}/I_G$ for each sample were analyzed and compared with values obtained for LIG from some other bioderived and synthetic precursors (Table S5, Supporting information). Based on the obtained results of Raman spectroscopy, it can be stated that in both cases (IR and UV scribing), LIG with a multilayer structure was obtained. However, according to the results of the $I_D/I_G$ ratios, the IR-LIG samples have a more chaotic planar structure compared to the UV-LIG samples. In both UV and IR cases, the $I_D/I_G$ ratios for S-ASC were lower than for H-ASC, which means that the LIG structure of S-ASC has a less defective structure and a higher graphitization degree. The $I_D/I_G$ ratio can also be used to evaluate the crystalline size, according to Equation (1) (Experimental Section), and it is found to be $L_a = 24$ nm and $L_a = 14$ nm for UV-LIG and IR-LIG from S-ASC, and $L_a = 17$ nm and $L_a = 13$ nm for UV-LIG and IR-LIG from H-ASC. In order to confirm the hypothesis that less crystalline carbon is formed deeper in the sample, as suggested during the discussion about Micro-CT observations, Raman spectra have also been collected on LIG created deeper inside the ASC. This was done by a simple experiment with tape: after laser scribing, a first Raman spectrum was obtained, then the topmost layer of LIG was removed using an adhesive tape, and a second Raman spectrum was obtained. From the spectra of this remaining LIG (Figure S8, Supporting Information), it is clear that the 2D band is absent, evidence of the presence of amorphous carbon.

### 2.4. ASC-LIG in Transient Electronics

#### 2.4.1. ASC-LIG Circuits

The direct and fast laser patterning of LIG on ASC allows the manufacturing of a variety of flexible electrical components and devices with desired geometries. Compared to other conducting materials commonly used in printed electronics, such as carbon-based and conducting polymer inks, the low sheet resistance of ASC-LIG makes it a good alternative to printed inks. Table S6 (Supporting Information) reports the sheet resistance values from the literature, evidencing the ASC-LIG readiness to be adopted as a valid substitute. To validate the wide applicability of LIG obtained from ASC, we fabricated different proof-of-concept designs of planar capacitors with interdigitated electrodes (**Figure 5a** left, top right). These can be used as proximity, pressure, humidity, or chemical sensors. Besides, conductive LIG traces can be used as interconnection lines, the equivalent of printed wires in printed electronics, such as in a circuit that lightens up an integrated LED (Figure 5a bottom right). Moreover, it is worth noting that the ASC has high heat resistance thanks to the ASP composition. This feature allows for soldering wires with tin, as is done for standard PCBs. As visible in Figure 5a (top right and bottom right inset), the tin soldering drop electrically connects the wire and the Ag-paste drop deposited onto the ASC-LIG without damaging it, even though a high temperature is locally reached. The possibility of soldering electrical components with tin directly on the ASC makes the biobased composite a promising green electronics substitute for standard plastic-based PCBs.

The resistivity of the ASC-LIG is also suitable for integrating resistors into circuits printed on the ASC to fabricate bioderived flexible boards. Figure 5b shows resistors of different geometries and combinations connected through printed silver tracks; the plot in Figure 5c reports the measured resistances sampled at $10^6$ Hz. The $R_1$ consists of a 10x5 $\text{mm}^2$ LIG rectangle with a resistance of 9180 ± 14 Ω, while the $R_2$ type resistor is a 5x5 $\text{mm}^2$ LIG square owing to a resistance of 432 ± 8.9 Ω. Other passive linear circuits (e.g., voltage dividers) can be created by either changing the geometry of individual resistive elements or combining them in series/parallel, with some examples shown in Figure 5b. The overall resistance $R_{tot}$ of different combinations of resistive elements is displayed in Figure 5c. In accordance with Ohm's law, when two resistors $R_2$ of 0.5 kΩ each are connected in series, a resistance ≈ 1 kΩ is measured, while the series combination of one $\text{R}_2$ with two $\text{R}_2$ resistors connected in parallel gives a slightly lower resistance value, among others. It is noteworthy that the production of graphene resistors through laser gives the possibility to tune the resistance values at will. Indeed, by means of different scribing parameters, one can obtain more or less dense and thick graphene and different combinations of graphene, graphite, and amorphous carbon/char. This approach finds high applicability in the development of specific flexible and transient electrical circuits from ASC, but it can be generalized to other bio-sourced substrates, which are LIG precursors.[3] Altogether, these examples demonstrate the use of LIG-based electrical components for the tailoring of potentially sustainable and degradable circuit boards.

#### 2.4.2. ASC and ASC-LIG Wettability and Water Uptake

Since some perspective applications of ASC and ASC-LIG in environmental sensing could include the interaction with liquid water and/or moisture, we characterized their wettability and water uptake properties. The results of CA measurements, summarized in Figure S9 (Supporting Information), reveal a distinct difference between the pristine S-ASC (top and bottom sides) and the ASC-derived UV- and IR-LIG. Both ASC and LIG produced from it are prone to wicking, and this significantly affects the CA dynamics. However, in the case of S-ASC, the water uptake is slower, and the CA measurements reveal hydrophobic behavior (CA > 90°) for both top and bottom surfaces. A progressive reduction of CA over time is observed from $t_0 = 0$ s CA = 98.32 ± 4.60° and CA = 95.33 ± 2.33°, to $t_1 = 30$ s CA = 84.48 ± 4.96° and CA = 85.95 ± 4.27° for top and bottom surfaces, respectively.

In the case of LIG, water wicking is more evident. At short time ($t_0 = 0$ s), UV-LIG has a more pronounced hydrophobicity with an apparent CA = 101.2 ± 3.32° to be compared with CA = 76.40 ± 8.56° obtained for IR-LIG. These results are in line with the wettability behavior of PI-LIG.[69] As discussed in the cited study, these results of apparent CA and the difference observed between UV- and IR-LIG can be ascribed to the combined effect of surface chemistry (presence of oxygen defects, polar groups), surface roughness, and porosity. Water wicking is, however, prevailing, and the droplet rapidly disappears in a few seconds, making any meaningful CA measurement impossible after 30 s (Figure S9 and Video S1, Supporting Information). The water absorption has been quantitatively assessed in dedicated experiments by measuring the mass change of rounded samples after soaking in water, and the results are reported in Figure S10 (Supporting Information). We estimated the ASC, the UV-LIG, and the IR-LIG to absorb up to ≈ 49.6,13.8, and 11.6%, respectively, of their initial weight.

#### 2.4.3. ASC-LIG Electrochemical Properties

As previously discussed, the ASC and the ASC-LIG both show a heterogeneous structure with different levels of porosity. This characteristic suggests functional electrochemical properties of this novel material when introduced in an aqueous environment. To investigate this aspect, we performed electrochemical impedance spectroscopy (EIS) of 1 $\text{cm}^2$ ASC-LIG electrodes (Figure S11a, Supporting Information), obtained from soft ASC through UV laser scribing. The Bode plot of a representative sample reported in Figure 5d shows an impedance modulus of $|Z|$ ≈ 1 kΩ at high frequencies ($\nu = 10^6$ Hz) and a higher modulus at lower frequencies. We found a resistive-capacitive behavior

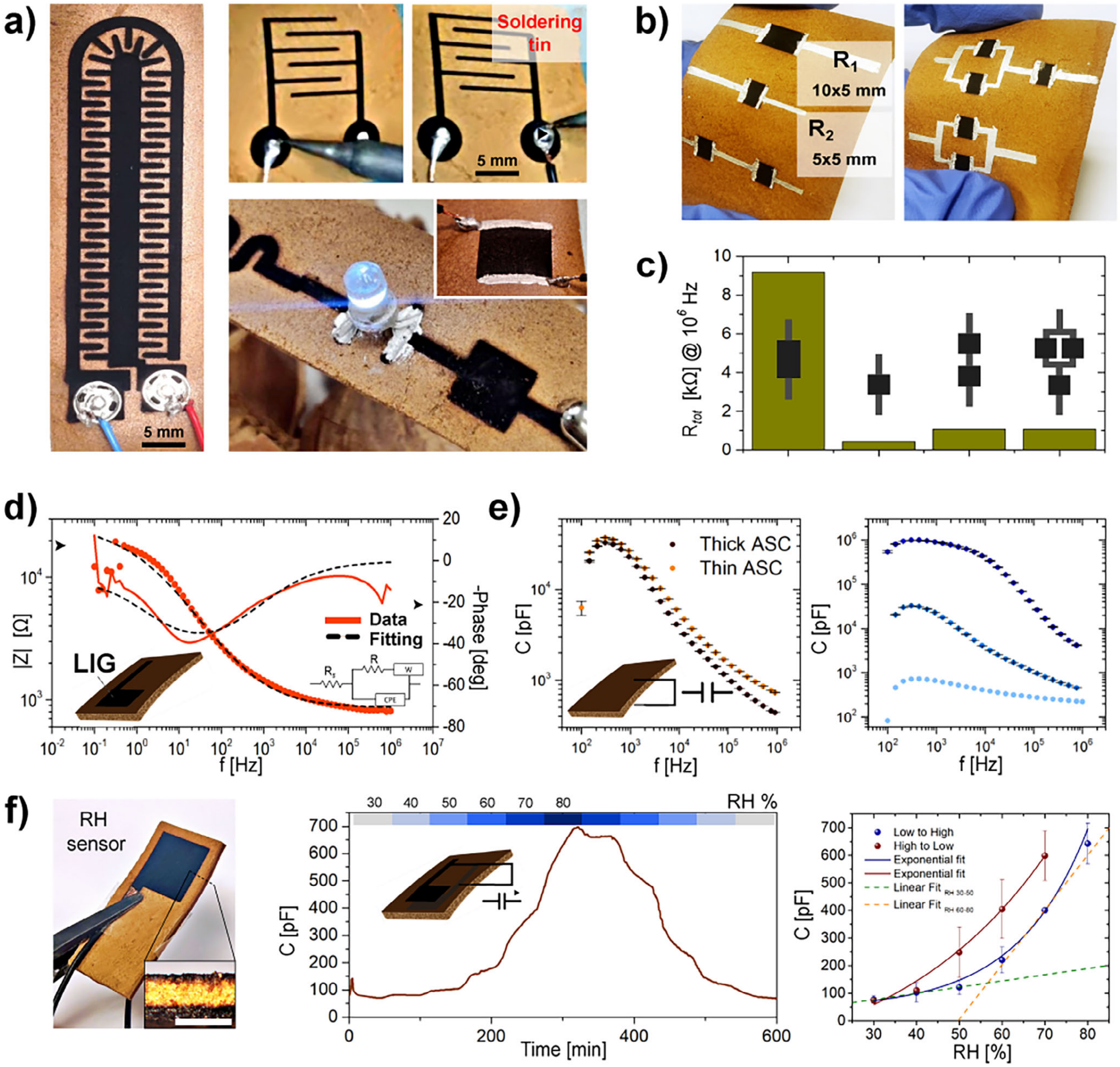

**Figure 5.** Application of ASC-LIG in flexible transient electronics. a) Proof-of-concept designs of planar capacitors with interdigitated LIG electrodes with snap button interconnection (left), of a planar capacitor with wires soldered with tin as interconnectors (top right), and of LIG connectors in a circuit with an LED (bottom right). b) Series of LIG resistors of different sizes and circuit configurations. c) Measurements of the total resistance of the circuits with LIG resistive elements are displayed in Figure 5b. d) Experimental and fitted data of the electrochemical impedance spectroscopy, modulus, and phase, of a 1 $cm^2$ ASC-LIG electrode. e) Capacitance (C) values over frequency of 1 $cm^2$ S-ASC sample. Left: comparison of the C between thin (600 µm) and thick (1.2 mm) samples measured at ambient conditions. Right: comparison of the C of a thick sample at different dry, ambient, and wet conditions. The plotted data are the averages and the standard errors of measurements repeated three times. f) ASC-LIG vertical capacitive RH sensor. Left: photo of the sensor together with its cross-section view. The scale bar in the inset represents 1 mm. Center: capacitance C vs time of the Humidity sensor when exposed to variable RH conditions. Right: RH sensor calibration curve within the RH range of 30%–80%. The plotted data are the average and the standard error of three tests.

that slightly differs from the EIS spectrum of a LIG electrode obtained from polyimide (Figure S11b, Supporting Information), considered as a standard. Polyimide-derived LIG (PI-LIG) electrode shows a resistive behavior for $10^1 < \nu < 10^6$ Hz and a capacitive one for $10^{-1} < \nu < 10$ Hz. In the case of PI-LIG, the EIS data can be fitted with an equivalent circuit composed of a resistor representing the electrolyte bulk resistance ($R_S$), and a resistor and capacitor in parallel, representing respectively the electrode charge-transfer and ionic double layer capacitance. Differently, the ASC-LIG electrode impedance can be fitted with a modified Randles circuit[70] (inset of Figure 5d). Here, the $R_S$ is in series with the parallel combination of a constant phase element (CPE) and a resistance (R) in series with a Warburg (W) element. The CPE and W elements, respectively, model the imperfect double-layer capacitance and the mass transfer diffusion resistance of the heterogeneous and more porous structure of the ASC-LIG electrode. Comparable EIS spectra and equivalent circuits are found in screen-printed carbon electrodes and paper-based LIG electrodes,[71,72] widely used in electrochemistry applications, suggesting a great potential of the ASC-LIG electrodes as a sustainable alternative in this field of application. For instance, a three-electrode cell can be scribed to develop a three-electrode sensor, as the layout reported in Figure S12a (Supporting Information) is commonly used for printed sensors as point-of-care devices. Furthermore, thanks to the high resolution and precision of the laser, one can fabricate miniaturized patterns as visible in Figure S12b (Supporting Information) for high-resolution and complex electronic systems.

#### *2.4.4. ASC-LIG-Based Humidity Sensor*

The urgent call for more sustainable electronics demands the implementation of a more environmentally friendly triad of the materials' origin, processing, and disposal. When considering carbon-based conducting materials, the most adopted solution is the printing of petroleum-derived carbon inks. In this framework, LIG appears as a potentially more sustainable alternative.[73]

In this work, we propose a fully biobased ASC-LIG relative humidity (RH) sensor. The ASC shows variable dielectric properties upon exposure to different humidity conditions, making it a suitable candidate as a substrate material for an RH capacitive sensor. First, we measured the capacitance at ambient conditions from $10^2$ to $10^6$ Hz of a thin (600 µm) and thick (1.2 mm) S-ASC square (1 $cm^2$) (Figure 5e left). The measurements on ASC capacitors resulted in relative permittivity values of $\varepsilon_r = 1058$ and $\varepsilon_r = 1438$ (at $10^5$ Hz, Figure S13, Supporting Information) for thin and thick samples, respectively. The granular structure of ASC allows a certain water absorption, which is expected to cause a change in the capacitance. We evaluate this change by measuring the capacitance of ASC (thick) samples at varying moisture levels (see Experimental Section, ASC-LIG circuits, and RH sensor). Figure 5e (right) reports the corresponding plots where the capacitance is at its minimum when the ASC is in fully dry conditions (light blue line). When the ASC sample is kept in ambient conditions, we expect it to absorb some water from the environment. The hygroscopic behavior is confirmed by the increase in capacitance (blue line, ambient condition). Whereas, when the ASC is completely wet, meaning its water uptake reaches the saturation condition, the measured capacitance is at maximum (dark blue line). This comparison confirms the progressive capacitance increase in direct correlation with the water amount absorbed by the ASC. Considering the correlation between the ASC capacitance and water amount, we designed a vertical capacitive RH sensor. Two LIG squares (1 $cm^2$) are scribed on both sides of a thick ASC sample (Figure 5f left) to act as the parallel plates between the ASC dielectric material of the vertical capacitor. As visible in the sensor cross-section photo, upon LIG scribing on both ASC faces, the ASC dielectric thickness results to be around 470 µm. The capacitance at ambient conditions of this sensor is found to be frequency-related within the range of $10^2$–$10^4$ Hz (Figure S14, Supporting Information). To test the response of the sensor to RH changes, we monitored the capacitance changes at 1 kHz while varying the RH at constant temperature (20 °C). The sensors exhibit a variable capacitance upon exposure to RH, as found in other literature works.[74–76] Specifically, the sensors signal increases and decreases with ramping the RH from low-to-high and high-to-low values, respectively. The time vs. capacitance graph (Figure 5f, center) reports the continuous sensor response and shows the reversibility of the ASC dielectric changes when exposed to variable conditions in the humidity. The sensor calibration curve (Figure 5f, right) evidences an exponential dependence between RH conditions and sensor output. To determine the sensor sensitivity, data are fitted with two linear regressions (Figure 5f, green and orange dashed lines). The sensor response within the RH range of 30%–55% is well fitted with a linear regression ($R^2 = 0.99$) that gives a sensitivity of 2.25 ± 0.13 pf %$RH^{-1}$. While within the RH range of 55%–80%, the linear regression ($R^2 = 0.96$) determines a higher sensitivity of 19.8 ± 2.69 pf %$RH^{-1}$. By comparing the sensor output when ramping RH from low-to-high and high-to-low values (Figure 5f, right, blue and red dots respectively), we observed a comparable signal within the RH range of 30%–50% and a slight signal hysteresis within the RH range 60%–80%. We attribute this behavior to the higher water amount absorbed by the ASC at higher RH: the rate of water desorption inside the ASC voids is lower, as a result of a slower equilibrium state process. The design and dimensions of the sensor play a crucial role in determining its response velocity. A direct approach lies in decreasing the LIG electrode size to increase the sensor response speed and reduce the hysteresis. A comparison between the ASC-LIG RH sensor and previously reported LIG-based RH sensors is provided in Table S7 (Supporting Information). The proposed RH sensor is flexible, degradable, and fabricated with a low-cost process. All together, these features make it an ideal candidate for applications such as environmental and plant monitoring. Specifically, RH and soil water availability represent key environmental factors to monitor in crop plants. Indeed, unbalanced local levels of humidity negatively impact the healthy growth of plants.[74,77] Lately, there has been a high interest in the implementation of novel technologies and transient electronic devices into this field to move toward digital agriculture to optimize water use and increase yields.

## 3. Conclusion

In this work, a novel almond shell-based composite was developed and subjected to laser-induced pyrolysis to obtain LIG. Two types of ASP (soft and hard shells cultivars) were investigated as waste biomass to be included in composites with a chitosan-based matrix. S-ASP, containing 38.7 ± 0.40% cellulose and 30.6 ± 0.34% lignin, was selected as the most suitable precursor for the synthesis of ASC with further conversion to LIG, as it provided the lowest sheet resistance while maintaining good mechanical properties of the material. The ASC composites showed good degradation profiles in soil, highlighting their potential as substrates for bioderived transient electronics. The laser scribing process was investigated with both UV and IR laser scribing systems. The combined Micro-CT and SEM analysis showed that the LIG structure obtained by UV laser was more porous and multilayered with respect to the one obtained by IR laser. A top porous layer with a thickness up to 120 µm is obtained for UV, which makes it ideal for sensor applications.

ASC-LIG was tested for the fabrication of flexible electronics and sensors. Resistors, capacitors, and interconnect lines for printed circuit boards were successfully produced. The electrical properties of ASC-LIG make it suitable for use as an electrode in various applications, including sensors and batteries. In addition, a proof-of-concept humidity sensor based on ASC-LIG was developed, showing good sensitivity to changes in humidity. Such a sensor, being flexible, fully bioderived, degradable, and inexpensive, can be used in environmental monitoring, for example, for agriculture.

Overall, this study highlights the potential of ASC and ASC-LIG as part of a circular economy approach. By repurposing an agricultural by-product into functional and degradable electronic substrate and components-possibly used in agriculture: from field to field-this work contributes to reducing electronic waste and promoting the use of potentially sustainable materials in next-generation technologies.

## 4. Experimental Section

*Materials*: Glycerol (≥99.5% CAS No. 56-81-5), glacial acetic acid (> 99% CAS No. 64-19-7), chitosan (chitosan medium molecular weight, deacetylated chitin, poly(D-glucosamine) CAS No. 9012-76-4), hexane (CAS-No. 110–54–3), ethanol (CAS No. 64-14-5), sulfuric acid (96%, CAS No. 7664–3–9), sodium chlorite (80%, CAS No. 7758–19–2) and sodium hydroxide (≥97.0%, 1310-73-2) were purchased from Sigma–Aldrich, and used without further modifications. Deionized water was obtained with the Millipore Elix Advantage 10 Water Purification System. Almond shells of two types from different almond cultivars (soft type – Vairo cultivar, hard type – Filippo Ceo) were obtained from Damiano S.p.A. The shells were grinded with a coffee grinder (Amazon Basics, CG9402-UL, max power 150 W) and sieved with Endecott 200SIW106 Stainless Steel Test Sieve system (certification ISO 3310-1) to obtain two almond shell powder (ASP) types (Hard ASP, Soft ASP) having a granulometry of < 50 µm, for chemical composition part the almond shells were ground with a LORDS XTRA GRINDING MACHINE (brand XTRA, power 2060 Watt), powder average particle size was 500 µm.

*Almond Shell Chemical Composition*: Lignin, cellulose, and hemicellulose in hard and soft almond shell types were extracted and determined using the characterization method for wood composition reported by Sluiter et al.[78] and Lengerr et al.[79] and for non-wood biomass by Álvarez et al.,[80]with some modifications.[81] Ground ASP (average particle size of 500 µm) was washed with distilled (DI) water and dried in the oven at 45 °C for 24 h until a constant weight was achieved. First, 10 g of ASP was placed in a Soxhlet apparatus and extraction was carried out using hexane as a solvent to remove lipids and fats, for 6 h at the boiling point of the solvent (68 °C). Then the ASP was washed in boiling water for 3 h with constant stirring, maintaining a constant volume, rinsed two times with water, then dried for 12 h at 50 °C, obtaining almond shell extractive-free biomass (ASP-EFB). Then, to separate the components, ASP-EFB was treated with a strong acid ($H_2SO_4$) using the Klason method.[38] This action destroyed the cellulose and hemicellulose molecules, leaving lignin as a dark solid. Briefly, sulfuric acid $H_2SO_4$ 72% (w/w) was added to the ASP sample for 20 min and then stirred for 2 h at 18–20 °C. The mixture was maintained in an ice bath to maintain a constant temperature, despite the exothermic reaction. After this, the whole mixture with $H_2SO_4$ was diluted with water up to 3% (v/v) in a 100 mL Erlenmeyer flask and boiled for 4 h while maintaining a constant volume (by periodically adding a pre-prepared 3% v/v $H_2SO_4$ solution). After the reaction, the sample was filtered, and the remaining solid precipitate (mainly lignin) was washed and dried in the oven at 50 °C. The exact mass of lignin was determined by drying in a desiccator and repeating the drying and weighing until the weight became constant. The second step was to determine the content of cellulose and hemicellulose remaining dissolved in the filtrate. 1% $NaClO_2$ was added to the filtrate, then the mixture was stirred continuously (with a magnetic stirrer) at 80 °C for 4 h. Acetic acid was added to the mixture to keep the pH between 4 and 5 to oxidize the lignin residues and isolate holocellulose, which consisted of cellulose and hemicellulose. The residual material resulting from holocellulose extraction was added to a 2% NaOH solution and stirred for 1 h at 80 °C to hydrolyze the hemicellulose chains and obtain cellulose as a white solid. The resulting cellulose was rinsed with water, dried, weighed, and its percentage in the original sample was calculated. The percentage of hemicellulose was determined by the difference in weight of holocellulose and cellulose, while the residual hydrolysis material was isolated after precipitation with a mixture of ethanol and acetic acid (5% v/v). The procedure was performed on three samples for each ASP type. A schematic of the extraction process is provided in Figure S15 (Supporting Information).

*Preparation of Almond Shell-Based Composites*: Almond shell composite (ASC) was prepared according to the method described in Figure 2a.

The first mixture was prepared by mixing 3.2 g of glycerol, 12.8 mL of DI water, and 64 mL of 2% acetic acid (AA). In the second mixture, 2 g of chitosan powder was mixed with 40 mL of 2% AA solution, since acidic pH promoted the dissolution of chitosan.[82] Both mixtures were stirred separately for 20 min at room temperature and then blended. The resulting mixture was continuously stirred for 1 h until the chitosan was completely dissolved. Then, 4 g of ASP (particle size < 50 µm) was added to the mixture, which constituted 2/3 of the total powder mass. The final mixture was stirred with a magnetic stirrer for 15 h at room temperature. The resulting solution was poured into a square Petri dish and dried in an oven at 45 °C for 6 h and then in air at room temperature for 12 h. The resulting composite film (typical thickness $t \approx 600$ µm, as measured with a digital caliper) was carefully removed from the Petri dish (size $n = 120$ mm × 120 mm). For the realization of ASC-LIG circuits and sensors described in the application part, thicker samples ($t \approx 1.2$ mm) were prepared, using the same chemical amounts but casting the mixture in a smaller Petri dish (circular shape, radius 45 mm).

A chitosan film was prepared as a reference using the same synthesis process and ingredient amounts as the ASC, but without adding ASP. The two mixtures (3.2 g of glycerol, 12.8 mL DI water with 64 mL 2% AA, and 2 g of chitosan with 40 mL 2% AA) were stirred separately for 20 min at room temperature, then combined and mixed on a magnetic stirrer for 16 h. The mixture was then poured into a Petri dish as for ASC. After drying, the resulting film had a thickness $t \approx 0.3$ mm.

It is worth noting that the synthesis procedure was optimized. Different formulations were systematically tested by adjusting the relative amounts of glycerol, shell powder, and chitosan (Figure S16, Supporting Information). A critical balance between the filler, matrix, and plasticizer contents that minimized phase separation and ensured structural homogeneity during the synthesis process was identified. This formulation was then consistently used for all the experiments.

*Laser Scribing*: The LIG was created on the surface of ASC in two ways. In the first case, LIG was scribed with an IR laser cutter/engraver (Universal Laser Systems VLS 3.50, $Pmax = 50$ W, laser emission wavelength $\lambda = 10.6$ µm) equipped with a 2.0 beam collimator (nominal beam size 130 µm) under ambient conditions. The IR laser was operated in raster mode with different parameter ranges to optimize the LIG resistivity: power $P = 5\%–20\%$, speed $S = 5\%–30\%$, dots per inch $PPI = 500$, image density $ID = 5$ (defining an interval between consecutive raster lines of 280 µm), and laser beam focus $Z = (0–5)$ mm. To optimize the focusing conditions and find the best set of laser scribing parameters, a continuous defocus sweep was applied through a 3D printed wedge/sample holder with a 5° tilt that could accommodate 75 × 25 mm$^2$ samples, with a procedure described elsewhere.[4,65] Also, the number of repetitions of scribing varied to achieve the lowest sheet resistance ($R_s$), measured with a source measure unit (SMU, Keithley 2604B) in two probes configuration: 1 cm$^2$ of ASC-LIG was scribed, silver paste contacts (CI-1036, Marabu) were manually painted at two of the sides of the square and cured at 70 °C. The resistance was measured by contacting the 2 SMU probes from the silver contacts. The best performance for the IR laser scribing was found at 3 repetitions.

In the second case, the LIG was scribed with a UV laser galvo scribing system (Keyence MD-U1000C, *Pmax* = 2.5 W, laser emission wavelength $\lambda = 355$ nm, nominal beam size 2 µm) under ambient conditions. The UV laser was operated in fill mode (in cross patterning along consecutive x and y directions, left->right, right->left), with different parameter ranges to optimize the LIG resistivity: $P = 10\%–30\%$, $S = 5–10$ mm s$^{-1}$, Q-switch frequency continuous wave CW = 100 kHz, fill interval = 0.025 mm, and laser beam focus $Z = 0$ mm, i.e., in focused state.

*Microscopic Morphology*: The microstructure and morphology of ASC and the derived LIG were investigated with a digital optical microscope (Hirox HR 5000 (E)) equipped with a High-Range Motorized Triple Zoom Lens, and with an SEM (Phenom XL, ThermoFisher Scientific) equipped with EDS/EDX and operating at 5 kV acceleration voltage.

For granulometry tests, S-ASP and H-ASP samples ($m = 8$ mg) were dispersed in deionized water (800 µL) with a vortex mixer (Velp Scientifica, CLASSIC Advanced Vortex Mixer) and an ultrasound cleaner (Branson, 2510). A droplet of the dispersed solution (30 µL) was placed on a glass slide and covered with a microscope slide cover glass, and right after, observed at the optical microscope. An automatic shape recognition system software tool of the optical microscope was used to assess the average diameter of the ASP. The particle size distribution was normalized over the total number of particles for each sample and averaged over three samples. Alternatively, the diameter was used to evaluate the volume of the particle (approximated as a sphere), and the volume distribution was normalized over the total volume of particles for each sample and averaged over three samples. Normalizing before averaging ensures that each sample contributes equally to the final distribution, regardless of differences in total particle volume.

The Raman spectroscopy was carried out with a LabRAM HR Evolution Raman microscope at a wavelength of $\lambda_i = 532$ nm, with a power percentage of 3.2% (nominal power = 3.2 mW). An integration time of 3 s per 15 accumulations, a slit size of 300 µm, and a × 100_VIS objective were used. The obtained raw data were then post-processed with peak-conservative smoothing, baseline correction, normalization on the $I_G$ peak, and averaged (over at least three samples). The peak ratios $I_D/I_G$ and $I_{2D}/I_G$ were obtained from the post-processed spectra. The $I_D/I_G$ ratio was used to evaluate the crystalline size, according to Equation (1).

$$L_a\,(nm) = \left(2.4 \cdot 10^{-10}\right) \lambda_i^4 \left(\frac{I_D}{I_G}\right)^{-1} \qquad (1)$$

*Composite Degradation Tests*: Tests of materials degradability in soil were conducted by burying ASC samples (disks, diameter 20 mm, thickness 0.6 mm) in soil and evaluating their weight loss (WL) at different time points over 90 days at room temperature. The tests were carried out in polypropylene pots filled with 200 g of all-purpose potting soil (organic substrate obtained from the local market), moisturized with 25 mL of tap water. For every time point, a set of three samples was weighed, freeze-dried at −80 °C for 48 h, and weighed again. The dry weights at time $t_0 = 0$ days were accounted for as $W_0$. The sets were then buried in the pots at a soil depth of 50 mm from the pot top on a previously placed fabric grid (this was done to make it easier to locate the samples in the soil after the decomposition test), and then the soil was covered with a punched aluminum foil to avoid excessive soil drying during the test.

At each time point ($t_1 = 2$ days, $t_2 = 8$ days, $t_3 = 20$ days, $t_4 = 40$ days, $t_5 = 90$ days), the samples were unburied and gently cleaned by brushing to remove soil residuals. For more thorough cleaning, the samples were then rinsed with water and soaked in 15 mL of deionized water and sonicated for 15 min, this procedure was repeated three times. Excess water was removed from wet samples with paper, then freezing at −80 °C (24 h), then freeze-dried at −80 °C for 48 h and weighed ($W_t$). The WL was calculated according to Equation (2).

$$WL\,(\%) = \frac{W_0 - W_t}{W_0} \cdot 100 \qquad (2)$$

To inspect the effects of degradation, samples at each time point were dried in a vacuum for at least 1 h, and SEM images and FTIR spectra were recorded with a Shimadzu IR Affinity-1 instrument equipped with a universal ATR (Attenuated Total Reflection) accessory (MIRacle 10). Each sample was uniformly pressed against the crystal surface using a spring-loaded anvil. Mid-IR spectra were obtained by averaging 64 scans over the wavenumber range 4000–600 cm$^{-1}$ at 4 cm$^{-1}$ resolution.

*Mechanical Test*: An Instron 5965 series universal testing machine equipped with a 1 kN load cell was employed for mechanical properties assessment, coherently with ASTM D882 standards. For mechanical tests, soft-type, hard-type, and chitosan film samples (dogbones) with ASTM D882 standard (sample width 5 mm, length 10 cm) were prepared in three pieces each. The thickness of the S-ASC and H-ASC samples was around 0.6 mm, and the thickness of the chitosan samples was around 0.3 mm. Before mechanical tests, the samples were placed in a climatic chamber overnight ($T = 25$ °C, humidity = 60%) to preserve the structure. A single tensile elongation at break test was carried out at 5 mm min$^{-1}$. The elongation at break values were evaluated as the maximum elongation reached before breaking.

*Micro-CT Measurement and Evaluation*: Micro-CT scans were performed using the UniTOM HR device (TESCAN ORSAY HOLDING, Brno, Czech Republic). The samples were mechanically cut and introduced into a Kapton tube with a 2 mm inner diameter. The acceleration X-ray voltage was set to 60 kV, and the target current was 108 µA for all the scans in a micro-focus mode. No filter was used to harden the beam. For each scan, 1749 projections were acquired with an angular range of 360°. Each projection was taken with a DEXELA camera with an exposure of 1.1 s, seven averages, and a two-times binning. The camera's pixel matrix and the geometrical magnification of ≈124.7 resulted in an isotropic voxel size of 1.2 µm. Each scan's field of view was ≈1.39 mm x 0.9 mm. The scans were reconstructed with the Panthera (TESCAN XRE) software (Ghent, Belgium) using a ring filter with a width of 10. The Dragonfly 3D World Software (Version 2024.1, Comet Technologies Canada Inc.) was used to evaluate the microstructure. The different layers were segmented using Otsu's thresholding algorithm, which is available in Dragonfly software.

*ASC-LIG Circuits and Sensor*: The LIG circuit elements, resistors, and planar capacitors, and the LIG electrode for electrochemical characterization were obtained through UV laser irradiation ($P = 18\%$, $S = 5$ mm s$^{-1}$, Q-switch frequency = 100 kHz, $Z = 0$) on 1.2 mm thick S-ASC samples by laser scribing on the bottom side. A commercial silver paste (CI-1036, Murabu) was manually deposited to pattern highly conducting tracks and interconnections between the LIG elements and the electronic readout. The ASC-LIG circuit elements were characterized with a source measurement unit (Keithley 2604B). The electrochemical impedance spectroscopy (EIS) of the ASC-LIG and PI-LIG squared ($n$ = 1 cm$^2$) electrodes was measured with a potentiostat (Gamry Instruments 45082) using a glass Ag/AgCl reference electrode and a platinum mesh as the counter electrode. Three ASC-LIG (UV) electrodes were tested. The PI-LIG electrode used as a reference in EIS was obtained on a 50 µm thick polyimide (Kapton, DuPont) foil by UV laser scribing ($P = 15\%$, $S = 20$ mm s$^{-1}$, Q-switch frequency = 210 kHz, $Z = 0$). The ASC-LIG and PI-LIG electrodes were immersed in 10 mM phosphate buffer saline and conditioned for 10 min before performing the EIS measurement. The EIS recording was set in potentiometric mode with an applied sinusoidal signal of 10 mV within a frequency range of $10^{-1}$–$10^{6}$ Hz. The equivalent circuit EIS data fitting was calculated with AfterMath software (Pine Research Instrumentation).

The capacitance of ASC thin (0.6 mm) and thick (1.2 mm) 1 cm$^2$ samples was measured with an LCR meter (BK Precision 895) within the frequency range of $10^2$–$10^6$ Hz before storing the samples at ambient conditions ($T \approx 20$ °C and $RH \approx 70\%$). Analogously, the capacitance of the ASC sample labeled as dry, ambient, and wet was obtained, respectively, after keeping the sample in the oven at 50 °C for 2 h first, keeping it at ambient conditions for 2 h later, and soaking it in deionized water for 1 h lastly. Three measurements were collected from the sample for each condition. The relative permittivity $\varepsilon_r$ at ambient conditions was calculated according to Equation (3).

$$\varepsilon_r = \frac{Cd}{A\varepsilon_0} \tag{3}$$

where C is the measured capacitance value, $d$ is the thickness of the ASC, $A$ is the ASC sample area, and $\varepsilon_0$ is the permittivity of free space.

To estimate the ASC and ASC-LIG water uptake capacity, a puncher was used to cut round (5 mm in diameter) specimens. Five specimens were used for each sample type: ASC, ASC-LIG UV, and ASC-LIG IR. These were kept in the oven at 50 °C for 2 h and weighed. Then they were kept dipped in deionized water for 2 h and weighed again before removing the water in excess, with absorbent paper, gliding on the samples' surface. The water contact angle measurements were performed on S-ASC (top and bottom surface) and ASC-LIG (UV and IR scribed) with a tensiometer (Biolin Theta Flex Optical tensiometer) using the sessile drop technique with droplets of deionized water with a volume of 5 µL. Samples were attached to glass slides with a double-sided adhesive to prevent bending due to water uptake/swelling. The measurements were repeated 3 times for each type of sample. The contact angle (CA) was measured with the One Attension software. Given the change of CA due to the rapid uptake of water, the CA was evaluated for 30 s, and values are given at $t_0 = 0$ s (right after the micropipette dispensed the droplet) and at $t_1 = 30$ s.

The RH sensor was obtained by scribing a square ($n = 1\ \text{cm}^2$) of LIG on both sides of a 1.2 mm thick S-ASC specimen. To characterize the sensor, it was placed inside a climatic chamber (ESPEC 242 SH) and connected to an LCR meter (BK Precision 895). The temperature was fixed at 20 °C while the RH was ramped from 30% to 80% (low-to-high) and from 80% to 30% (high-to-low) with steps of 10%, composed of 10 min ramping and 50 min steady state condition. The sensor calibration curve was obtained by sampling the sensor output (capacitance C) at each RH step (50 min). The sensor response test was repeated three times.

## Supporting Information

Supporting Information is available from the Wiley Online Library or from the author.

## Acknowledgements

This work was dedicated to the memory of Dr. Giuseppe Lenzo from Damiano S.p.A., whose passionate work and discussion with F.G. provided the seed of inspiration for the project. The authors thank Dr. Virgilio Mattoli for lending the instruments to characterize the ASC-LIG sensors and humidity sensors, Dr. Laura M. Ferrari for the inputs on the capacitance measurements, Dr. Francesca Pignatelli for the use of FTIR, and Riccardo Damiano, Mariateresa Licata, and Letizia Tropeano from Damiano S.p.A. for the fruitful collaboration and the supply of almond shells. Y.S., A.C.B., M.G., and F.G. acknowledged funding received by LIGASH Project, jointly funded by Damiano S.p.A. and the Italian Ministry of Education and Research, MUR, in the framework of the Fund for the promotion and development of policies of the National Research Program PNR, coherently with EU Regulation n. 241/2021 and with PNRR 2021–2026. F.G. and H.G.B. acknowledged the support of the BRIEF "Biorobotics Research and Innovation Engineering Facilities" project (Project identification code IR0000036) funded under the National Recovery and Resilience Plan (NRRP), Mission 4 Component 2 Investment 3.1 of the Italian Ministry of University and Research, funded by the European Union- NextGenerationEU. M.G., A.C.B., and F.G. acknowledged the support of the PNRR- Investment 1.5 Ecosystems of Innovation, Project Tuscany Health Ecosystem (THE), Spoke 3 "Advanced technologies, methods, materials and health analytics" CUP: I53C22000780001. A.C.B. acknowledged funding of PhD grant from Programma Operativo Nazionale – PON "Green" Research and Innovation (CCI 2014IT16M2OP005) from the Ministry of Education, University and Research, Italy, and FSE React-EU.

## Conflict of Interest

The authors declare no conflict of interest.

## Data Availability Statement

The data that support the findings of this study are available from the corresponding author upon reasonable request.

## Keywords

almond shell waste, bioderived composite, biomass valorization, laser-induced graphene, sensors

Received: March 24, 2025
Revised: June 6, 2025
Published online:

---

[1] J. Lin, Z. Peng, Y. Liu, F. Ruiz-Zepeda, R. Ye, E. L. G. Samuel, M. J. Yacaman, B. I. Yakobson, J. M. Tour, *Nat. Commun.* **2014**, *5*, 5714.
[2] P. I. C. Claro, T. Pinheiro, S. L. Silvestre, A. C. Marques, J. Coelho, J. M. Marconcini, E. Fortunato, L. H. C. Mattoso, R. Martins, *Appl. Phys. Rev.* **2022**, *9*, 041305.
[3] A. C. Bressi, A. Dallinger, Y. Steksova, F. Greco, *ACS Appl. Mater. Interfaces* **2023**, *15*, 35788.
[4] S. T. Sankaran, A. Dallinger, A. C. Bressi, A. Marino, G. Ciofani, A. Szkudlarek, V. Bilovol, K. Sokolowski, B. Kunert, H. K. Hampel, H. G. Bernal, F. Greco, *Small* **2024**, *20*, 2405252.
[5] H. Moon, B. Ryu, *Int. J. Precis. Eng. Manuf.-Green Tech.* **2024**, *11*, 1279.
[6] R. Ye, D. K. James, J. M. Tour, *Adv. Mater.* **2019**, *31*, 1803621.
[7] H. Huang, H. Shi, P. Das, J. Qin, Y. Li, X. Wang, F. Su, P. Wen, S. Li, P. Lu, F. Liu, Y. Li, Y. Zhang, Y. Wang, Z.-S. Wu, H.-M. Cheng, *Adv. Funct. Mater.* **2020**, *30*, 1909035.
[8] H. Yoon, J. Nah, H. Kim, S. Ko, M. Sharifuzzaman, S. C. Barman, X. Xuan, J. Kim, J. Y. Park, *Sens. Actuators, B* **2020**, *311*, 127866.
[9] S. Nandy, S. Goswami, A. Marques, D. Gaspar, P. Grey, I. Cunha, D. Nunes, A. Pimentel, R. Igreja, P. Barquinha, L. Pereira, E. Fortunato, R. Martins, *Adv. Mater. Technol.* **2021**, *6*, 2000994.
[10] A. Dallinger, K. Keller, H. Fitzek, F. Greco, *ACS Appl. Mater. Interfaces* **2020**, *12*, 19855.
[11] G. De Luca, A. C. Bressi, M. Maselli, F. Greco, M. Cianchetti, presented at *2024 46th Ann. Int. Conf. of the IEEE Engineering in Medicine and Biology Society (EMBC)*, Orlando, FL, USA, July **2024**, https://doi.org/10.1109/EMBC53108.2024.10782696.
[12] F. Vivaldi, A. Dallinger, N. Poma, A. Bonini, D. Biagini, P. Salvo, F. Borghi, A. Tavanti, F. Greco, F. Di Francesco, *APL Bioeng.* **2022**, *6*, 036104.
[13] H. Wang, Z. Zhao, P. Liu, Y. Pan, X. Guo, *ACS Appl. Mater. Interfaces* **2022**, *14*, 41283.
[14] G. De Luca, A. C. Bressi, R. Pathan, N. Pagliarani, M. Maselli, F. Greco, M. Cianchetti, *Adv. Int. Syst.* **2025**, https://doi.org/10.1002/aisy.202401071.
[15] L. Cheng, W. Guo, X. Cao, Y. Dou, L. Huang, Y. Song, J. Su, Z. Zeng, R. Ye, *Mater. Chem. Front.* **2021**, *5*, 4874.
[16] V. P. Wanjari, A. S. Reddy, S. P. Duttagupta, S. P. Singh, *Environ. Sci. Pollut. Res.* **2023**, *30*, 42643.

[17] R. Ye, Y. Chyan, J. Zhang, Y. Li, X. Han, C. Kittrell, J. M. Tour, *Adv. Mater.* **2017**, *29*, 1702211.
[18] T. Pinheiro, M. Morais, S. Silvestre, E. Carlos, J. Coelho, H. V. Almeida, P. Barquinha, E. Fortunato, R. Martins, *Adv. Mater.* **2024**, *36*, 2402014.
[19] C. Zhou, Y. Wang, *Sci. Technol. Adv. Mater.* **2020**, *21*, 787.
[20] X. Xu, M. Zhang, C. Qi, Y. Sun, L. Yang, X. Gu, Y. Li, M. Wu, B. Wang, H. Hu, *Green Chem.* **2025**, *27*, 959.
[21] J. S. Jayan, S. S. Jayan, *Adv. Eng. Mater.* **2023**, *25*, 2300248.
[22] F. Mahmood, Y. Sun, C. Wan, *RSC Adv.* **2021**, *11*, 15410.
[23] Y. Wang, M. Zhang, X. Shen, H. Wang, H. Wang, K. Xia, Z. Yin, Y. Zhang, *Small* **2021**, *17*, 2008079.
[24] D. H. Vieira, E. Carlos, M. S. Ozório, M. Morais, E. Fortunato, N. Alves, R. Martins, *Adv. Int. Syst.* **2025**, *7*, 2400760.
[25] C. H. Dreimol, H. Guo, M. Ritter, T. Keplinger, Y. Ding, R. Günther, E. Poloni, I. Burgert, G. Panzarasa, *Nat. Commun.* **2022**, *13*, 3680.
[26] C. H. Dreimol, R. Kürsteiner, M. Ritter, A. Parrilli, J. Edberg, J. Garemark, S. Stucki, W. Yan, S. Tinello, G. Panzarasa, I. Burgert, *Small* **2024**, *20*, 2405558.
[27] V. Silva, I. Oliveira, J. A. Pereira, B. Gonçalves, *Plants* **2024**, *13*, 540.
[28] R. Meadows, *ACS Cent. Sci.* **2023**, *9*, 2171.
[29] Almond Almanac 2024 - The Almond Board of California, at https://www.almonds.com/sites/default/files/2024-12/Digital_Almanac_2024.pdf (accessed: July 2025).
[30] V. K. Singh, G. Bansal, P. Negi, A. Bisht, *J. Test. Eval.* **2017**, *45*, 763.
[31] A. Ibáñez García, A. Martínez García, S. Ferrándiz Bou, *Polymers* **2020**, *12*, 2049.
[32] R. Ben Arfi, A. Ghorbal, *Euro-Mediterr. J. Environ. Integr.* **2024**, *9*, 545.
[33] M. G. Plaza, C. Pevida, C. F. Martín, J. Fermoso, J. J. Pis, F. Rubiera, *Sep. Purif. Technol.* **2010**, *71*, 102.
[34] A. Omri, M. Benzina, N. Ammar, *J. Ind. Eng. Chem.* **2013**, *19*, 2092.
[35] A. Kali, A. Amar, I. Loulidi, M. Jabri, C. Hadey, H. Lgaz, A. A. Alrashdi, F. Boukhlifi, *Biomass Conv. Bioref.* **2024**, *14*, 3655.
[36] L. Landucci, R. A. Smith, S. Liu, S. D. Karlen, J. Ralph, *Energy Fuels* **2020**, *34*, 16274.
[37] C. Manterola-Barroso, D. Padilla Contreras, G. Ondrasek, J. Horvatinec, G. Gavilán CuiCui, C. Meriño-Gergichevich, *Plants* **2024**, *13*, 1034.
[38] C. S. G. P. Queirós, S. Cardoso, A. Lourenço, J. Ferreira, I. Miranda, M. J. V. Lourenço, H. Pereira, *Biomass Conv. Bioref.* **2020**, *10*, 175.
[39] X. Li, Y. Liu, J. Hao, W. Wang, *Materials* **2018**, *11*, 1782.
[40] B. T. Iber, N. A. Kasan, D. Torsabo, J. W. Omuwa, *J. Renew. Mater.* **2021**, *10*, 1097.
[41] J. Chen, L. Yan, W. Song, D. Xu, *Composites, Part A* **2018**, *114*, 149.
[42] M. Çalışkan, T. Baran, *J. Organomet. Chem.* **2022**, *963*, 122284.
[43] A. Kartik, D. Akhil, D. Lakshmi, K. Panchamoorthy Gopinath, J. Arun, R. Sivaramakrishnan, A. Pugazhendhi, *Bioresour. Technol.* **2021**, *329*, 124868.
[44] X. Wang, M. Tarahomi, R. Sheibani, C. Xia, W. Wang, *Int. J. Biol. Macromol.* **2023**, *241*, 124472.
[45] G. F. Schutz, S. de Ávila Gonçalves, R. M. V. Alves, R. P. Vieira, *Int. J. Biol. Macromol.* **2024**, *261*, 129916.
[46] H. P. S. Abdul Khalil, E. W. N. Chong, F. a. T. Owolabi, M. Asniza, Y. Y. Tye, S. Rizal, M. R. Nurul Fazita, M. K. Mohamad Haafiz, Z. Nurmiati, M. T. Paridah, *J. Appl. Polym. Sci.* **2019**, *136*, 47251.
[47] C. Larrigy, M. Burke, A. Imbrogno, E. Vaughan, C. Santillo, M. Lavorgna, L. Sygellou, G. Paterakis, C. Galiotis, D. Iacopino, A. J. Quinn, *Adv. Mater. Technol.* **2023**, *8*, 2201228.
[48] A. Beltrán Sanahuja, S. E. Maestre Pérez, N. Grané Teruel, A. Valdés García, M. S. Prats Moya, *Foods* **2021**, *10*, 153.
[49] S. Rivas, A. Moure, J. C. Parajó, *Agronomy* **2020**, *10*, 760.
[50] S. Wang, C. Zou, H. Yang, C. Lou, S. Cheng, C. Peng, C. Wang, H. Zou, *Bioresour. Technol.* **2021**, *320*, 124375.
[51] E. Maftuah, M. Saleh, E. Pratiwi, *IOP Conf. Ser.: Mater. Sci. Eng.* **2020**, *980*, 012064.
[52] A. Khouaja, A. Koubaa, H. Ben Daly, *Chemosphere* **2025**, *379*, 144415.
[53] A. Ghavipanjeh, S. Sadeghzadeh, *Sci. Rep.* **2024**, *14*, 4475.
[54] A. Ghavipanjeh, S. Sadeghzadeh, *Comput. Mater. Sci.* **2024**, *244*, 113240.
[55] J. Berglund, D. Mikkelsen, B. M. Flanagan, S. Dhital, S. Gaunitz, G. Henriksson, M. E. Lindström, G. E. Yakubov, M. J. Gidley, F. Vilaplana, *Nat. Commun.* **2020**, *11*, 4692.
[56] L. Zhang, H. Lu, J. Yu, Z. Wang, Y. Fan, X. Zhou, *J. Agric. Food Chem.* **2017**, *65*, 9587.
[57] M. Ramos, F. Dominici, F. Luzi, A. Jiménez, M. C. Garrigós, L. Torre, D. Puglia, *Polymers* **2020**, *12*, 835.
[58] A. Ibáñez, S. Ferrándiz, A. Martínez, *IOP Conf. Ser.: Mater. Sci. Eng.* **2021**, *1193*, 012015.
[59] A. Ibáñez-García, A. Martínez-García, S. Ferrándiz-Bou, *Waste Biomass Valor.* **2021**, *12*, 5823.
[60] B. Shi, Z. Hao, Y. Du, M. Jia, S. Xie, *BioResources* **2024**, *19*, 4001.
[61] J. R. Shivanna, M. Manisha, A. Srinivas, B. Baldevraj, E. K. Nandini, A. Srivastava, *J. Sci. Ind. Res.* **2021**, *80*, 949.
[62] B. Piro, H. V. Tran, V. T. Thu, *Sensors* **2020**, *20*, 5898.
[63] L. W. Hartman, E. M. Andrews, E. G. Galatis, A. C. M. Gaudin, P. H. Brown, S. D. S. Khalsa, *Soil Systems* **2024**, *8*, 51.
[64] N. Wrońska, N. Katir, M. Nowak-Lange, A. El Kadib, K. Lisowska, *Foods* **2023**, *12*, 3519.
[65] M. Abdulhafez, G. N. Tomaraei, M. Bedewy, *ACS Appl. Nano Mater.* **2021**, *4*, 2973.
[66] H. Hamidi, J. Levieux, C. Larrigy, A. Russo, E. Vaughan, R. Murray, A. J. Quinn, D. Iacopino, *Biosens. Bioelectron.: X* **2023**, *15*, 100403.
[67] R. Nandee, M. A. Chowdhury, A. Shahid, N. Hossain, M. Rana, *Results Eng.* **2022**, *15*, 100474.
[68] R. Murray, M. Burke, D. Iacopino, A. J. Quinn, *ACS Omega* **2021**, *6*, 16736.
[69] A. Dallinger, F. Steinwender, M. Gritzner, F. Greco, *ACS Appl. Nano Mater.* **2023**, *6*, 16201.
[70] N. O. Laschuk, E. Bradley Easton, O. V. Zenkina, *RSC Adv.* **2021**, *11*, 27925.
[71] Q. Liu, Q. Shi, H. Wang, Q. Zhang, Y. Li, *RSC Adv.* **2015**, *5*, 47074.
[72] G. Bhattacharya, S. J. Fishlock, S. Hussain, S. Choudhury, A. Xiang, B. Kandola, A. Pritam, N. Soin, S. S. Roy, J. A. McLaughlin, *ACS Appl. Mater. Interfaces* **2022**, *14*, 31109.
[73] J. Edberg, R. Brooke, O. Hosseinaei, A. Fall, K. Wijeratne, M. Sandberg, *npj Flex. Electron.* **2020**, *4*, 17.
[74] J. M. Nassar, S. M. Khan, D. R. Villalva, M. M. Nour, A. S. Almuslem, M. M. Hussain, *npj Flex. Electron.* **2018**, *2*, 24.
[75] Z. Li, J. Wang, Y. Xu, M. Shen, C. Duan, L. Dai, Y. Ni, *Carbohydr. Polym.* **2021**, *270*, 118385.
[76] X. Zhao, Y. Long, T. Yang, J. Li, H. Zhu, *ACS Appl. Mater. Interfaces* **2017**, *9*, 30171.
[77] S. Yin, H. Ibrahim, P. S. Schnable, M. J. Castellano, L. Dong, *Adv. Mater. Technol.* **2021**, *6*, 2001246.
[78] J. B. Sluiter, R. O. Ruiz, C. J. Scarlata, A. D. Sluiter, D. W. Templeton, *J. Agric. Food Chem.* **2010**, *58*, 9043.
[79] S. K. Lengger, L. Neumaier, L. Haiden, M. Feuchter, T. Griesser, J. Kosel, *Sustainable Mater. Technol.* **2024**, *40*, 00936.
[80] A. Álvarez, S. Cachero, C. González-Sánchez, J. Montejo-Bernardo, C. Pizarro, J. L. Bueno, *Carbohydr. Polym.* **2018**, *189*, 250.
[81] M. Salgado-Ramos, F. J. Martí-Quijal, A. J. Huertas-Alonso, M. P. Sánchez-Verdú, F. J. Barba, A. Moreno, *Ind. Crops Prod.* **2022**, *179*, 114697.
[82] I. A. Sogias, V. V. Khutoryanskiy, A. C. Williams, *Macromol. Chem. Phys.* **2010**, *211*, 426.